
Philosophical Magazine

ISSN: 1478-6435 (Print) 1478-6443 (Online) Journal homepage: http://www.tandfonline.com/loi/tphm20

Hardening mechanisms in olivine single crystal deformed at 1090 °C: an electron tomography study

Alexandre Mussi, Patrick Cordier, Sylvie Demouchy & Benoit Hue

To cite this article: Alexandre Mussi, Patrick Cordier, Sylvie Demouchy & Benoit Hue (2017) Hardening mechanisms in olivine single crystal deformed at 1090 °C: an electron tomography study, Philosophical Magazine, 97:33, 3172-3185, DOI: 10.1080/14786435.2017.1367858

To link to this article: http://dx.doi.org/10.1080/14786435.2017.1367858

PHILOSOPHICAL MAGAZINE, 2017
VOL. 97, NO. 33, 3172–3185
https://doi.org/10.1080/14786435.2017.1367858

Hardening mechanisms in olivine single crystal deformed at 1090 °C: an electron tomography study

Alexandre Mussi[a], Patrick Cordier[a], Sylvie Demouchy[b] and Benoit Hue[a]

[a]Unité Matériaux et Transformations, UMR 8207 CNRS – Université Lille1, Villeneuve d'Ascq, France; [b]Géoscience Montpellier, UMR 5342 CNRS – Université Montpellier, Montpellier, France

ABSTRACT

The dislocation microstructures in a single crystal of olivine deformed experimentally in uniaxial compression at 1090 °C and under a confining pressure of 300 MPa, have been investigated by transmission electron tomography in order to better understand deformation mechanisms at the microscale relevant for lithospheric mantle deformations. Investigation by electron tomography reveals microstructures, which are more complex than previously described, composed of [0 0 1] and [1 0 0] dislocations commonly exhibiting 3D configurations. Numerous mechanisms such as climb, cross-slip, double cross-slip as well as interactions like junction formations and collinear annihilations are the source of this complexity. The diversity observed advocates for microscale deformation of olivine significantly less simple than classic dislocation creep reported in metals or ice close to melting temperature. Deciphering mechanism of hardening in olivine at temperatures where ionic diffusion is slow and is then expected to play very little role is crucial to better understand and thus model deformation at larger scale and at temperatures (900–1100 °C) highly relevant for the lithospheric mantle.

ARTICLE HISTORY
Received 20 March 2017
Accepted 8 August 2017

KEYWORDS
Olivine; plastic deformation; dislocations; electron tomography; cross-slip; climb

1. Introduction

Cooling of the Earth is mediated by convection processes, which induces plastic deformation of mantle rocks at extremely slow strain rates. As the upper mantle is principally composed of olivine (>60% in volume), this mineral controls the mechanical properties of the Earth's upper mantle. In this study, we investigate the plastic behaviour of olivine at the temperature of 1090 °C (i.e. a temperature similar to those near the lithosphere/asthenosphere boundary). At this temperature and for grain size >1 mm, dislocation creep is expected to be the dominant mechanism of plastic deformation, with potentially contribution of dislocations with [1 0 0] and [0 0 1] Burgers vectors. Indeed, deformation in the [0 1 0] direction

CONTACT Alexandre Mussi alexandre.mussi@univ-lille1.fr

has never been reported for olivine (i.e. the so-called olivine paradox [1]). Below 1000 °C, olivine deforms by glide along [0 0 1] [2–6] while above 1200 °C [1 0 0] glide dominates [3,7–9]. A [0 0 1]/[1 0 0] transition temperature of approximately 1000 °C was reported by Raleigh [10], where the dislocation microstructures of deformed olivine seem to be complex. Indeed, Durham et al. [3] and Raterron et al. [8,9] have observed 3D shapes [1 0 0] and [0 0 1] dislocations in their samples. The behaviour of olivine single crystals deformed experimentally below 1000 °C has already been investigated yielding a mechanical data-set [11] together with transmission electron microscopy (TEM) observations [12,13]. Most of the deformed samples did not reach steady state, and deformation curves exhibit continuous hardening. Two samples were particularly interesting: specimen PoEM9 deformed at ~800 °C and specimen PoEM11, deformed at 850 °C. Only [0 0 1] dislocations have been reported in theses samples, but yet the dislocation microstructure, imaged by TEM was complex, as evidenced by several dislocation loop families and numerous 3D-dislocations. Furthermore, for polycrystalline olivine, deformed at higher temperature (900 °C, sample PoEM22 and 21), TEM analyses have demonstrated the occurrence of a majority of [0 0 1] dislocations with only few [1 0 0] [14]. A more recent study, also based on experimentally deformed olivine single crystals, but deformed in simple shear and at temperature ranging from 1000 and 1300 °C, has reported a transition temperature of approximately 1200 °C [15]. This mechanical study was completed by sample characterisation using electron backscatter diffraction (EBSD), but no TEM analyses were performed.

The aim of the present study is to further elucidate how dislocations interact to generate or not hardening during plastic deformation of olivine above 1000 °C, but below 1200 °C, where temperature is yet not high enough to induce significant ionic diffusion and recovery/annealing processes. We use the experimentally deformed samples from Demouchy et al. [11] and TEM for dislocation characterisations using up-to-date electron tomography to accurately understand how 3D-dislocations microstructures are produced. Electron tomography of dislocations allows overcoming the intrinsic limitations of observation of dislocation microstructures in the TEM (due to limitations in tilt amplitude) and ultimately provides a 3D numerical model of the dislocations geometries. These geometrical parameters (line directions, planes containing the lines in relation with the Burgers vectors) are very important to decipher the actual mechanisms operating in a deformed olivine.

2. Experimental methods

2.1. Description of the specimens and the deformation experiments

Olivine single crystals (from, San Carlos, AZ, USA) were deformed at 300 MPa in a confining medium of argon [16,17]. Prior to deformation, olivine cylinders were crystallographically oriented parallel to $[1\ 0\ 1]_c$ (i.e. the direction at 45° between [1 0 0] and [1 0 0] in the orthorhombic cell of olivine) to activate the

[0 0 1](1 0 0), [0 0 1](1 1 0), [1 0 0](0 0 1) and [1 0 0](0 1 1) slip systems [11]. Two samples are investigated here: PoEM8 and again PoEM9. The experimental conditions are summarised on Table 1. Technical details are fully reported in [11]. In brief, samples were deformed in axial compression at a constant displacement rate. Resulting deformation curves show large flow stresses (final stress of 754 and 498 MPa for PoEM9 and PoEM8, respectively), where steady state was not reached since a constant hardening was observed. At the end of the experiments, the deformation piston was maintained in place, and the temperature decreased (i.e. 'slow quench') at a rate of 150 °C/min. Recovered samples were cut parallel to the compression axis in two sections, two slabs located in the centre part of the section were prepared for EBSD and TEM characterisation, respectively. Sample preparation specific for electron tomography is detailed below.

2.2. Transmission electron tomography

Thin slabs were cut from the deformed specimen and mechanically polished down to a thickness of 30 μm. In order to reach electron transparency, the sample foils were Ar-ion milled with a Gatan® DuoMill TM model 600. Carbon films were deposited on the thin foils to ensure electron conduction. TEM investigations were performed with a FEI® Tecnaï G^{2}20Twin microscope, operating at 200 kV with a LaB$_6$ filament, using a double tilt sample-holder with a maximal angular range of ±60°. Olivine crystal structure is orthorhombic ($a \approx 4.75$Å, $b \approx 10.19$Å and $c \approx 5.98$Å). It is described here within a *Pbnm* space group [18]. The diffraction patterns were simulated with the Electron Diffraction software, in kinematic conditions [19]. Dislocations were characterised using the weak-beam dark-field (WBDF) technique. The use of a precessed electron beam [20] enabled us to: (1) facilitate indexing of the diffraction pattern (with a large precession angle (>1°), multiple diffraction paths are limited, which enables us to get closer to kinematic conditions); (2) homogenise the background and the dislocation contrasts [21,22]; a precession angle of 0.1° is high enough to drastically reduce the thickness fringe contrasts and the dislocation oscillating contrasts as well as low enough to avoid masking the precessed beam by the objective aperture.

Five and seven tilted series were acquired, every 2°, in WBDF conditions associated with precession, from approximately −60° to 56° and −56° to 48° for PoEM8 and PoEM9, respectively. As the contrast is weak in WBDF, the acquired tilted series have been manually centred within one-pixel accuracy [22] using the Gatan® image alignment software. Each micrograph has been numerically filtered with a kernel matrix [23] and/or a polynomial fit, using the ImageJ software, to

Table 1. Experimental conditions for deformation of the two olivine single crystals.

Specimen	Temperature	Final stresses (MPa)	$\dot{\varepsilon}$	$\varepsilon_{\mathrm{Total}\,(\%)}$
PoEM9	806 °C	754	5.10^{-5} s^{-1}	10.1
PoEM8	1090 °C	498	10^{-5} s^{-1}	7.4

homogenise the background and the dislocation contrasts, and to increase the dislocation contrast. The weighted back projection algorithm [24] was used to reconstruct the dislocation volumes. This algorithm is accessible on the TomoJ plugin [25], which is available on ImageJ. Most dislocations have been redrawn using the UCSF Chimera software [26–28].

3. Results

3.1 Dislocation content

All the micrographs used for the tilted series of PoEM8 have been acquired in WBDF conditions with the $2\,2\,\bar{2}$ diffraction vector ($\boldsymbol{g}$). Five zones have been investigated, which represent an analysed volume of approximately 27 μm^3. A representative micrograph of PoEM8 is shown in Figure 1. Dislocations are curved; no straight dislocations (often taken as indicative of glide controlled by lattice friction) can be found. There are dislocations with [1 0 0] and [0 0 1] Burgers vectors which can be distinguished using $\boldsymbol{g} = 2\,2\,\bar{2}$ (Figure 1(a)) and $0\,6\,\bar{2}$ (Figure 1(b)). A few junctions are pointed out by yellow arrows (Figures 1, 2, 3 and 4). With

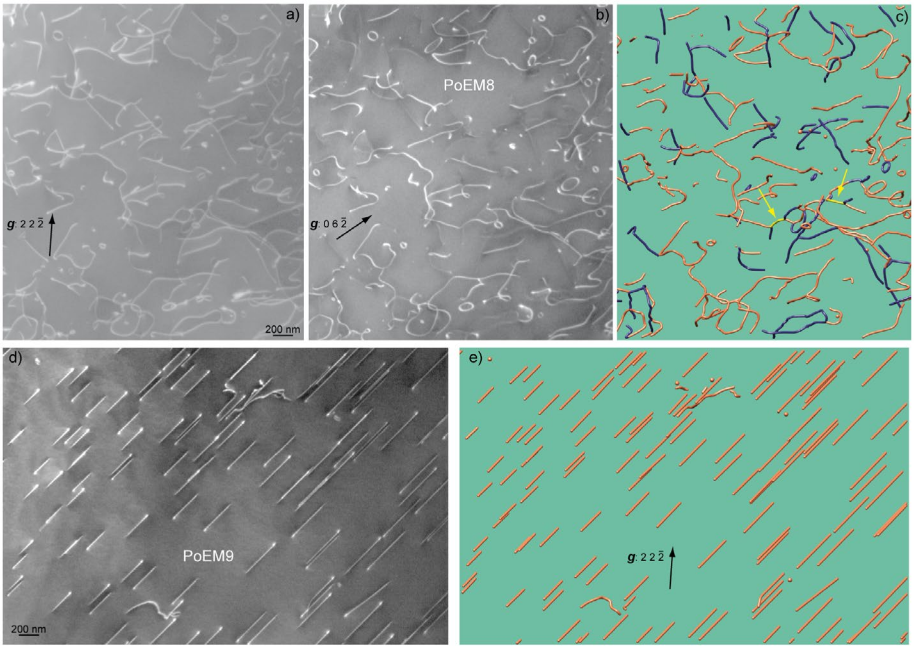

Figure 1. (Colour online) Typical PoEM8-PoEM9 microstructures: (a) WBDF micrograph obtained with the $2\,2\,\bar{2}$ diffraction vector ([1 0 0] and [0 0 1] dislocations are in contrast); (b) WBDF micrograph obtained with $\boldsymbol{g} = 0\,6\,\bar{2}$ on the same region as (a) (only [0 0 1] dislocations are in contrast); (c) Corresponding 3D reconstruction ([1 0 0], [0 0 1] and $[1\,0\,\bar{1}]$ dislocations are shown in blue, orange and yellow colours, respectively), the two yellow arrows point out $[1\,0\,\bar{1}]$ junctions; (d) Characteristic microstructure of PoEM9 only composed of [0 0 1] dislocations, with a large majority of straight lined screw segments, few non-screw segments and scarce dislocation loops [10]; (e) 3D reconstruction of (d) ([0 0 1] dislocations are shown in orange).

$\boldsymbol{g} = 2\,2\,\bar{2}$, the $[1\,0\,\bar{1}]$ junctions exhibit contrasts twice as bright as $[1\,0\,0]$ and $[0\,0\,1]$ segments. Indeed, the $\boldsymbol{g}{\cdot}\boldsymbol{b}$ product is equal to 4 for $b = [1\,0\,\bar{1}]$, and 2 for $b = [1\,0\,0]$ and $b = [0\,0\,1]$. The $[1\,0\,1]$ junctions are out of contrast as the $\boldsymbol{g}{\cdot}\boldsymbol{b}$ product is equal to 0 with $b = [1\,0\,1]$. In the reconstructed volume shown in Figure 1(c), orange, blue and yellow colours are used to differentiate dislocations with $[1\,0\,0]$, $[0\,0\,1]$ and $[1\,0\,\bar{1}]$ Burgers vectors, respectively. Small loops ($\emptyset \approx 30$ nm) and larger loops ($\emptyset_{max} \approx 250$ nm) of $[1\,0\,0]$ and $[0\,0\,1]$ dislocations are observed. Electron tomography has provided the possibility to index more than 1000 planes containing dislocation segments. They are reported in Table 2. The proportion of gliding[1] dislocations is close to 40% and approximately 70% of the whole indexed planes are composed of $[0\,0\,1]$ dislocation segments. The total dislocation density, which is calculated from the total dislocation length digitised in Chimera, is 2.6×10^{13} m^{-2}.

3.2. Dislocation distribution and slip systems

Electron tomography allows, by indexing the planes containing dislocation segments, to discriminate those in glide configurations (so-called 'gliding') from the sessile ones, as shown in Figure 2, where numerous dislocations from the $[0\,0\,1](1\,1\,0)$ and $[1\,0\,0](0\,0\,1)$ slip systems can be characterised. Dislocations belonging to the $[0\,0\,1](1\,1\,0)$ slip system are shown in white while those from $[1\,0\,0](0\,0\,1)$ are drawn in black. Considering all the tilted series (Table 2), we find that 76% of gliding dislocation belong to $[0\,0\,1]\{1\,1\,0\}$, whilst 16% belong to $[0\,0\,1](1\,0\,0)$. Over half of the gliding $[1\,0\,0]$ segments are lying in $(0\,0\,1)$. Moreover,

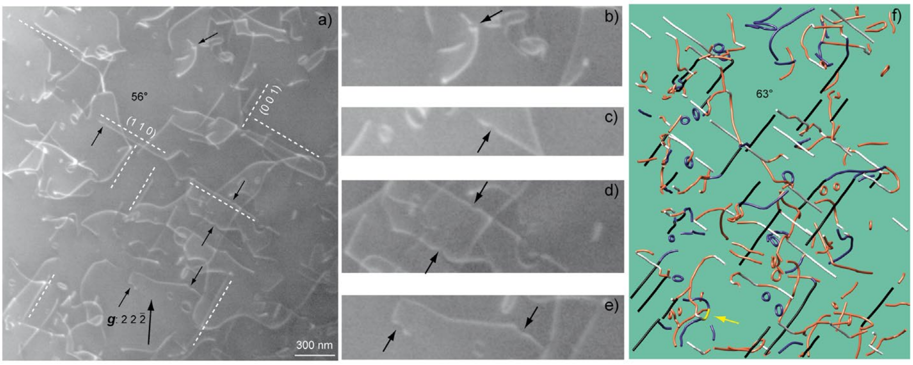

Figure 2. (Colour online) Main slip systems and cross-slip or/and collinear annihilations in PoEM8: (a) WBDF micrograph performed with $\boldsymbol{g} = 2\,2\,\bar{2}$, with a tilt angle of 56° where: the $(1\,1\,0)$ and the $(0\,0\,1)$ plane are indicated, black arrows point out probable specific configurations, which may be cross-slip or/and collinear interactions with small dislocation loops (some isolated loop, with approximately the same sizes, are in the vicinity); (b) Three Enlargement of (a), upper part; (c) Enlargement of (a), upper part of the image centre; (d) Enlargement of (a), lower part of the image centre; (e) Enlargement of (a), lower part; (f) Corresponding reconstruction volume, with a projected angle of 63° where: black dislocation segments designate the edge-on $[1\,0\,0](0\,0\,1)$ slip systems, white dislocation segments designate the edge-on $[0\,0\,1](1\,1\,0)$ slip systems, the yellow arrow points out a $[1\,0\,\bar{1}]$ junction.

a high proportion of dislocations from [1 0 0]{0 1 1} and [1 0 0]{0 2 3} slip systems are also observed. Since the angle between (0 1 1) and (0 2 3) is only of 9°, we have grouped them, and together they represent approximately one third of all the gliding [1 0 0] segments. We will now focus on the indexed planes, which cannot be related to gliding dislocations. Their role is important since they represent 60% of the indexed dislocations.

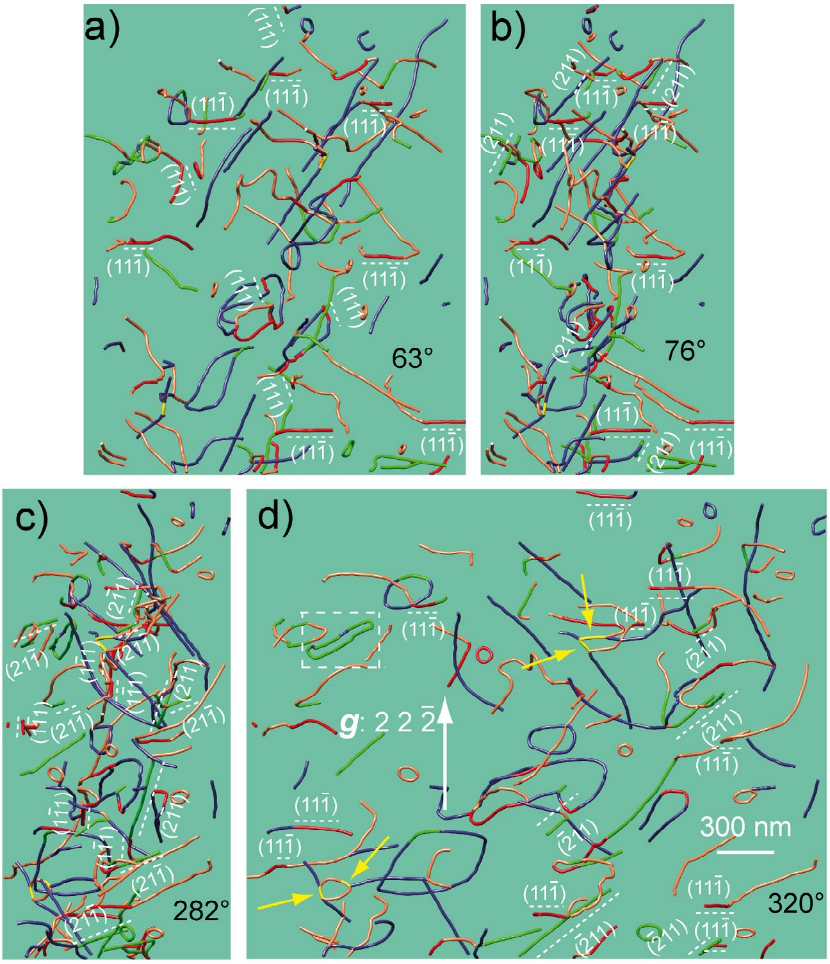

Figure 3. (Colour online) Dislocation climb planes (the dislocation segments which lie on the {1 1 1} planes are coloured in red and the dislocation segments are coloured in green for the {2 1 1} planes): (a) 3D reconstruction of a PoEM8 tilted series obtained with $\boldsymbol{g} = 2\,2\,\bar{2}$, with a projected angle of 63° (the $(1\,1\,\bar{1})$ and (1 1 1) planes are edge-on with this projection condition); (b) Projection angle of 76° (the $(1\,1\,\bar{1})$ and (2 1 1) planes are edge-on along this direction); (c) 282° tilt angle (the $(1\,1\,\bar{1})$, $(1\,\bar{1}\,1)$, $(2\,1\,\bar{1})$ and $(2\,\bar{1}\,1)$ planes are edge-on with this orientation); (d) Projection angle of 320° (the $(1\,1\,\bar{1})$ and $(\bar{2}\,1\,1)$ planes are edge-on with this projection condition), the white dashed square points out a break-up of a dislocation dipole by climb, the four yellow arrows point out $[1\,0\,\bar{1}]$ junctions; The numerous dislocation segments which lie on the {1 1 1} and the {2 1 1} planes (19 segments in {1 1 1} and 23 segments in {2 1 1}) show the occurrence of climb in PoEM8.

3.3. Sessile dislocation segments

There are a variety of indexed planes containing sessile dislocation segments, but several planes are more abundant (Table 2). A total of 25% of all planes containing sessile dislocation segments are members of the {1 1 1} family for both [1 0 0] and [0 0 1] Burgers vectors, 12% of [0 0 1] dislocations lie within (0 0 1). 9% of dislocations with [1 0 0] and [0 0 1] Burgers vectors lie within {2 1 1}. Consequently, approximately 50% of all the indexed planes of the sessile dislocations belong to {1 1 1}, (0 0 1) and {2 1 1}. The presence of numerous dislocation segments lying on {1 1 1} and {2 1 1} is clearly confirmed by Figure 3 (in red and green, respectively). The other indexed sessile dislocations are lying on odd {*hkl*} planes.

4. Discussion

4.1. Influence of temperature from 800 to 1090 °C (comparison between PoEM8 and PoEM9)

The compression axis of PoEM8 is along [10 4 19] and that of PoEM9 is along [1 0 1], i.e. at only 24° from each other. From a purely geometrical point of view, these two orientations are likely to activate the same slip systems, i.e. [0 0 1](1 0 0), [0 0 1](1 1 0), [1 0 0](0 0 1) and [1 0 0](0 1 1). The orientation alone is unlikely to be able to explain the marked differences between the dislocation microstructures observed in PoEM8 and in PoEM9 (Figure 1(d)–(e)). However, there is a difference of 300 °C between PoEM8 and PoEM9. Consequently, the comparison of these two experiments gives us the possibility to study the role of temperature in this range. The microstructure of PoEM9 is composed of [0 0 1] screw gliding dislocations only; while the microstructure of PoEM8 is mainly composed of non-screw, [1 0 0] and [0 0 1] dislocations, with 3D shapes and a large fraction of sessile components. The occurrence of [1 0 0] dislocations was expected in PoEM8, as the onset for [1 0 0] glide has already been reported in olivine above ca. 900–1000 °C in single crystals [2–4,8–10,15] and polycrystals [5,6,14,29,30]. Considering the Schmid factors associated with the slip systems in PoEM8, we find that [0 0 1]{1 1 0} and [1 0 0](0 0 1) are the most activated slip systems, followed by [0 0 1](1 0 0). As there are only [0 0 1] dislocations in PoEM9, the most activated slip systems are [0 0 1]{1 1 0}, followed by the [0 0 1](1 0 0) slip system [10].

The occurrence of large dislocation loops (several hundreds of nm), lying on undefined {*hkl*} planes, can be explained by the mechanism of double cross-slip [31]. Three configurations indicative of double cross-slip are found in PoEM8 as shown in Figure 4:

- the first configuration (Figure 4(a)) consists of a [0 0 1] dislocation, which double cross-slips on the (1 1 0) and $\left(1\,\bar{1}\,0\right)$ planes;
- the second configuration (Figure 4(b)) consists of a [1 0 0] dislocation, which double cross-slips on the (0 1 0) and (0 0 1) planes;

- and the third one, more complex (Figure 4(c)), consists of a [0 0 1] dislocation, which double cross-slips on the (1 1 0) and $(1\,\bar{1}\,0)$ planes, with an interaction with a [1 0 0] dislocation, notice a $[1\,0\,\bar{1}]$ junction as well.

This mechanism has already been mentioned in a previous study on the dislocation population characterisation in deformed sample PoEM11 (see Figure 5 in [13]). From Table 1, approximately half of sessile dislocation segments lie on unexpected $\{hkl\}$ planes. This seems to be the signature of a high occurrence of the double cross-slip mechanism in PoEM8.

The activation of [100] glide in PoEM8 may explain the difference of microstructure with PoEM9. [100] and [001] dislocations may interact and create sessile junctions which have already been predicted in olivine using Dislocation Dynamics simulations [32] and observed in TEM [12]. The observed 3D configurations may result from the need for entangled dislocations to find other degrees

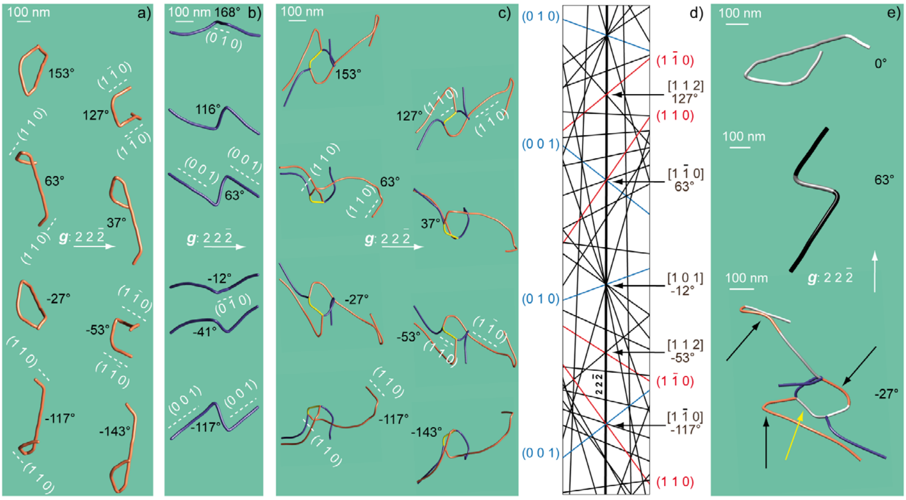

Figure 4. (Colour online) Double cross-slip mechanism: (a) Reconstructed volume of a [0 0 1] dislocation obtained with $\boldsymbol{g} = 2\,2\,\bar{2}$ (projected angle of −143°, −117°, −53°, −27°, 37°, 63°, 127° and 153°), the (1 1 0) planes are edge-on for the −117° and 63° tilt angles ($[1\,\bar{1}\,0]$ zone axis) and the $(1\,\bar{1}\,0)$ planes are edge-on for the −53° and 127° tilt angles ([1 1 2] zone axis); (b) Reconstructed volume of a [1 0 0] dislocation performed with the same diffraction vector as (a) (projected angle of −117°, −41°, −12°, 63°, 116° and 168°), the (0 0 1) planes are edge-on for the −117° and 63° tilt angles and the (0 1 0) planes are edge-on for the −12° and 168° tilt angles ([1 0 1] zone axis); (c) Complex dislocation configuration composed of a [1 0 0] and a [0 0 1] dislocation, a $[1\,0\,\bar{1}]$ junction (yellow segment) and an attractive [0 0 1]/[1 0 0] dislocation crossed state; moreover a double cross-slip configuration of the [0 0 1] dislocation is revealed (same description as (a)); (d) Simulation of the Kikuchi lines, between −165° and 180°, in kinematic conditions (Electron Diffraction Software [33]); the (0 1 0) and (0 0 1) Kikuchi lines are shown in blue colour (in reference with the [1 0 0] dislocation in blue colour) and the (1 1 0) and $(1\,\bar{1}\,0)$ Kikuchi lines are shown in red colour (in reference with the [0 0 1] dislocation in orange colour); (e) Summary of the three dislocation configurations in (a), (b) and (c) for tilt angles of 0°, 63° and −27°, respectively (the white dislocations segments designate the [0 0 1](1 1 0) slip systems, the light grey dislocations segments refer to the [0 0 1]$(1\,\bar{1}\,0)$ slip systems and the black dislocation segments designate the [1 0 0](0 0 1) slip systems), the yellow arrow points out a $[1\,0\,\bar{1}]$ junction.

Table 2. Lying planes for the [1 0 0] and [0 0 1] dislocations in sample PoEM8.

Dislocation	Mechanisms	{*hkl*} planes	Total
[0 0 1]	Glide	(1 0 0)	41
		{1 1 0}	199
		{1 2 0}	9
		{1 3 0}	1
		{1 4 0}	3
		(010)	7
	Climb	(0 0 1)	81
		{1 1 1}	114
		{211}	38
		{1 1 2}	47
	Unknown	{*hkl*}	220
[1 0 0]	Glide	(0 0 1)	79
		{0 2 3}	32
		{0 1 1}	16
		{0 2 1}	11
		{0 4 1}	8
		(0 1 0)	7
	Climb	{1 1 1}	48
		{2 1 1}	20
	Unknown	{*hkl*}	91
[0 0 1] proportion			71%
[0 0 1] glide proportion			34%
[1 0 0] glide proportion			49%
Glide proportion			39%
Climb Proportion			32%
Unknown proportion			29%
		Total	1072

of freedom to move (cross-slip and/or climb). Climb is another possibility as at 1090 °C (i.e. approximately 70% of the melting temperature of olivine), ionic diffusion mechanisms are expected to still play a role. Approximately half of all the indexed sessile planes correspond to odd {*hkl*} planes (arising from double cross-slip mechanisms), and almost half of all the indexed sessile planes correspond to {1 1 1}, (0 0 1) and {2 1 1} (Table 2). As these three sessile plane families have frequently been indexed, there is a strong possibility that they come from a specific mechanism like climb. Consequently, we propose that {1 1 1}, (0 0 1) and {2 1 1} could be climb planes. Due to the low deformation temperature of PoEM9, few dislocation segments in climb configurations, had been observed in this specimen [13]. However, Durham and coworkers [2,3] had already draw attention on the importance of climb mechanisms in olivine single crystals deformed in the temperature range 1150–1600 °C.

Generally, climb and cross-slip are expected to induce strain softening during plastic deformation [34]. However, the PoEM8 stress/strain curve shows strain hardening (Figure 3 in Demouchy et al. [11]), which we discuss below.

4.2. Strain hardening during the deformation of an olivine single crystal at 1090 °C

Taking into account the previously mentioned aspects, a scenario for the different mechanisms activated during the plastic deformation of an olivine single crystal deformed at 1090 °C is now proposed.

As soon as the yield stress is reached, [0 0 1] and [1 0 0] dislocations multiply to reach a ratio of ⅔ of [0 0 1] and ⅓ for [1 0 0] (Table 2). Easy slip systems, i.e. [1 0 0](0 0 1), [0 0 1]{1 1 0} and [0 0 1](1 0 0), are then active. As [1 0 0] and [0 0 1] dislocations glide on different planes, they interact and generate [1 0 1] and $\left[1\,0\,\bar{1}\right]$ junctions (see Figures 1(c), 2(c), 3 and 4(c)–(e)), which impede dislocation glide. Dipoles of [0 0 1] and $\left[0\,0\,\bar{1}\right]$ dislocations, and of [1 0 0] and $\left[\bar{1}\,0\,0\right]$ dislocations also form, which is potentially another source of strain hardening. From Boioli et al. [35], we know that these dipoles progressively annihilate by climb, generating small sessile dislocation loops (Ø < 30 nm). As a result of diffusion, these small loops progressively disappear, increasing the proportion of the largest ones [36]. As an illustration, such an elongated dislocation loop can be noted in Figure 3(d) (framed area). This loop appears to be a closed-ended dipole (as shown in the Figure 6 in Lagerlöf et al. [37]). Gliding dislocations may interact with such remaining loops and create [1 0 1] and $\left[1\,0\,\bar{1}\right]$ junctions as well as collinear interactions. [1 0 0] and [0 0 1] dislocations are both affected by collinear annihilations. Junctions formed by collinear interactions are difficult to unzip [38]. Consequently, collinear interactions represent a third potential mechanism of strain hardening. Even if there are several strain hardening mechanisms, dislocations can overcome obstacles and move using mechanisms other than glide, including climb, cross-slip and multiple cross-slip. However, these mechanisms can also promote locking mechanisms, as they create 3D dislocation structures. Multiple cross-slip and more precisely double cross-slip generates large dislocation loops with a diameter of several hundreds of nm, lying in unprescribed {*hkl*} planes [31], for dislocations with [0 0 1] and [1 0 0] Burgers vectors. As mentioned previously, gliding dislocations can interact with these sessile loops, inducing a fourth strong strain hardening contribution. Consequently, we find that numerous strain hardening mechanisms are potentially involved during the plastic deformation of PoEM8, which is in agreement with the compression stress–strain curve evolution displayed in Figure 3 in Demouchy et al. [11].

It is worth mentioning that the picture presented here corresponds to deformation tests performed at laboratory strain rates (of the order $10^{-5}\ \mathrm{s}^{-1}$, Demouchy et al. [11]), which are considerably faster than mantle strain rates (of the order of $10^{-14}\ \mathrm{s}^{-1}$). The macroscopic hardening is obviously the result of a dynamic process, which involves a competition between formation of obstacles to dislocation glide and recovery processes, which overcome them. As for sessile loops for instance, their elimination being controlled by ion and vacancy diffusion, one can expect that more time being provided in nature, their hardening role should be reduced. A first assessment of this issue has been presented in Boioli et al. [35]. As a result, strain hardening near the lithosphere/asthenosphere boundary may be less significant than suggested by experimental data.

5. Conclusion

The dislocation microstructure of PoEM8 (1090 °C) is more complex than in PoEM9 (~800 °C) and several mechanisms could explain the generation of these microstructures (e.g. collinear interaction, climb, and cross-slip) but their de-convolution is difficult. Nevertheless, electron tomography enables us to characterise the double cross-slip mechanism and the comparison between the two experiments (PoEM8 and PoEM9) helps to identify different interaction mechanisms: (1) PoEM9 has been deformed well below 1000 °C (at 806 °C). Its microstructure is principally composed of straight screw [0 0 1] dislocations highlighting high lattice friction at 800 °C. The orientation of the compression axis of PoEM9 preferentially activates the [0 0 1]{1 1 0} and [0 0 1](1 0 0) slip systems. Few dipoles appear during plastic deformation. As the climb mechanism is weakly activated at such a temperature, the creation of sessile dislocation loops by progressive dipolar annihilations is consequently limited. The low occurrence of dislocation loops reduces collinear interactions, so the dislocation microstructure of PoEM9 is simple. (2) PoEM8 was deformed at 1090 °C. Its microstructure is composed of both [1 0 0] and [0 0 1] dislocations. The [1 0 0](0 0 1), [0 0 1]{1 1 0} and [0 0 1](1 0 0) slip systems dominate the microstructure, in agreement with the orientation of the compression axis. Moreover, both diffusion, and climb did occur due to the more elevated temperature. Consequently, planar glide controlled by lattice friction is not dominant and the dislocation shapes become 3-dimensional. With such a configuration, many junctions and collinear interactions form during the deformation. Dislocations can get away from their blocked configurations by cross-slip. The mechanism of double cross-slip produces large sessile dislocation loops, sources of new dislocation interactions. Consequently, the dislocation microstructure of PoEM8 is more diverse and intricate than the microstructure of PoEM9, and permits to revise the mechanisms of plastic deformation in the peridotitic mantle, where grain size is too large and temperature is too low to lead to only diffusion creep. Here, at 1090 °C, ionic diffusion is still at play, but only as a secondary process, unlocking locally dislocations. This result will allow to better model plastic deformation of the uppermost mantle at larger scale for temperatures (900–1100 °C) highly relevant for the lithospheric mantle.

Note

1. By ‘gliding’ dislocations, we mean dislocations which are in glide configuration, i.e. where the plane containing the dislocation line also contains the Burgers vector. This is to be opposed to sessile dislocations, for which the Burgers vector is not in the plane containing the dislocation line. Hence these sessile dislocations cannot glide in their plane. Sessile dislocations can be produced by mechanisms like climb or cross-slip.

Acknowledgements

A Marie Curie fellowship awarded to S.D. (PoEM: Plasticity of Earth Mantle, FP7-PEOPLE-20074-3-IRG, N°230748-PoEM) supported the experimental work used in this study. The TEM national facility in Lille is supported by the CNRS (INSU) and the Conseil Régional du Nord Pas de Calais, France. We thank D. Wallis for a careful review of the manuscript, which has contributed to improve clarity.

Disclosure statement

No potential conflict of interest was reported by the authors.

Funding

This work was supported by the Marie Curie fellowship awarded to Sylvie Demouchy (PoEM: Plasticity of Earth Mantle, FP7-PEOPLE-20074-3-IRG) [grant number N°230748-PoEM]; the European Research Council within the Seventh Framework Program (FP7) [grant number N°290424] – RheoMan to Patrick Cordier.

ORCID

Alexandre Mussi http://orcid.org/0000-0003-2093-0144
Patrick Cordier http://orcid.org/0000-0002-1883-2994

References

[1] P. Cordier, S. Demouchy, B. Beausir, V. Taupin, F. Barou, and C. Fressengeas, *Disclinations provide the missing mechanism for deforming olivine-rich rocks in the mantle*, Nature 507 (2014), pp. 51–56.

[2] W.B. Durham and C. Goetze, *Plastic flow of oriented single crystals of olivine: 1. Mechanical data*, J. Geophys. Res. 82 (1977), pp. 5737–5753.

[3] W.B. Durham, C. Goetze, and B. Blake, *Plastic flow of oriented single crystals of olivine: 2. Observations and interpretations of the dislocation structures*, J. Geophys. Res. 82 (1977), pp. 5755–5770.

[4] P. Phakey, G. Dollinger, and J. Christie, *Transmission electron microscopy of experimentally deformed olivine crystals*, in *Flow and Fracture of Rocks, Geophysical Monograph Series*, H.C. Heard, I.Y. Borg, N.L. Carter, and C.B. Raleigh, eds., AGU, Washington, 1972, pp. 117–138.

[5] Y. Gueguen, *High temperature olivine creep: Evidence for control by edge dislocations*, Geophys. Res. Lett. 6 (1979a), pp. 357–360.

[6] Y. Gueguen, *Les dislocations dans l'olivine des péridotites*, PhD thesis, Université Nantes, Nantes, 1979b.

[7] O. Jaoul, M. Michaut, Y. Gueguen, and D. Ricoult, *Decorated dislocations in forsterite*, Phys. Chem. Miner. 5 (1979), pp. 15–19.

[8] P. Raterron, J. Chen, L. Li, D. Weidner, and P. Cordier, *Pressure-induced slip-system transition in forsterite: Single-crystal rheological properties at mantle pressure and temperature*, Am. Mineral. 92 (2007), pp. 1436–1445.

[9] P. Raterron, E. Amiguet, J. Chen, L. Li, and P. Cordier, *Experimental deformation of olivine single crystals at mantle pressures and temperatures*, Phys. Earth Planet. Inter. 172 (2009), pp. 74–83.

[10] C.B. Raleigh, *Mechanisms of plastic deformation of olivine*, J. Geophys. Res. 73 (1968), pp. 5391–5406.

[11] S. Demouchy, A. Tommasi, T.B. Ballaran, and P. Cordier, *Low strength of Earth's uppermost mantle inferred from tri-axial deformation experiments on dry olivine crystals*, Phys. Earth Planet. In. 220 (2013), pp. 37–49.

[12] A. Mussi, P. Cordier, and S. Demouchy, *Characterization of dislocation interactions in olivine using electron tomography*, Philos. Mag. 95 (2015a), pp. 335–345.

[13] A. Mussi, M. Nafi, S. Demouchy, and P. Cordier, *On the deformation mechanism of olivine single crystals at lithospheric temperatures: An electron tomography study*, Eur. J. Mineral. 27 (2015b), pp. 707–715.

[14] S. Demouchy, A. Mussi, F. Barou, A. Tommasi, and P. Cordier, *Viscoplasticity of polycrystalline olivine experimentally deformed at high pressure and 900 °C*, Tectonophysics 623 (2014), pp. 123–135.

[15] J.A. Tielke, M.E. Zimmerman, and D.L. Kohlstedt, *Direct shear of olivine single crystals*, Earth Planet. Sci. Lett. 455 (2016), pp. 140–148.

[16] M.S. Paterson, *A high pressure, high temperature apparatus for rock deformation*, Int. J. Rock Mech. Min. 7 (1970), pp. 512–517.

[17] M.S. Paterson, *Rock deformation experimentation*, in *The Brittle-Ductile Transition in Rocks: The Head Volume, Geophysical Monograph Series*, A.G. Duba, W.B. Durham, J.W. Handin, and H.F. Wang, eds., AGU, Washington, DC, 1990, pp. 187–194.

[18] R.M. Hazen, *Effects of temperature and pressure on the crystal structure of forsterite*, Am. Mineral. 61 (1976), pp. 1280–1293.

[19] J.P. Morniroli and J.W. Steeds, *Microdiffraction as a tool for crystal-structure identification and determination*, Ultramicroscopy 45 (1982), pp. 219–239.

[20] R. Vincent and P.A. Midgley, *Double conical beam-rocking system for measurement of integrated electron diffraction intensities*, Ultramicroscopy 53 (1994), pp. 271–282.

[21] J.M. Rebled, L. Yedra, S. Estradé, J. Portillo, and F. Peiró, *A new approach for 3D reconstruction from bright field TEM imaging: Beam precession assisted electron tomography*, Ultramicroscopy 111 (2011), pp. 1504–1511.

[22] A. Mussi, P. Cordier, S. Demouchy, and C. Vanmansart, *Characterization of the glide planes of the [0 0 1] screw dislocations in olivine using electron tomography*, Phys. Chem. Miner. 41 (2014), pp. 537–545.

[23] J.S. Barnard, A.S. Eggeman, J. Sharp, T.A. White, and P.A. Midgley, *Dislocation electron tomography and precession electron diffraction – minimising the effects of dynamical interactions in real and reciprocal space*, Philos. Mag. 90 (2010), pp. 4711–4730.

[24] G.T. Herman, A.V. Lakshminarayanan, and A. Naparstek, *Convolution reconstruction techniques for divergent beams*, Comput. Biol. Med. 6 (1976), pp. 259–271.

[25] C. Messaoudi, T. Boudier, C.O. Sanchez Sorzano, and S. Marco, *TomoJ (tomography software for three-dimensional reconstruction in transmission electron microscopy)*, 2007; software available at https://u759.curie.fr/fr/download/softwares/TomoJ.

[26] E.F. Pettersen, T.D. Goddard, C.C. Huang, G.S. Couch, D.M. Greenblatt, E.C. Meng, and T.E. Ferrin, *UCSF Chimera: A visualization system for exploratory research and analysis*, J. Comput. Chem. 25 (2004), pp. 1605–1612.

[27] G.S. Liu, S.D. House, J. Kacher, M. Tanaka, K. Higashida, and I.M. Robertson, *Electron tomography of dislocation structures*, Mater. Charact. 87 (2014), pp. 1–11.

[28] A. Mussi, P. Cordier, S. Ghosh, N. Garvik, B.C. Nzogang, P. Carrez, and S. Garruchet, *Transmission electron microscopy of dislocations in cementite deformed at high pressure and high temperature*, Philos. Mag. 96 (2016), pp. 1773–1789.

[29] L. Li, D. Weidner, P. Raterron, J. Chen, M. Vaughan, M. Shenghua, and B. Durham, *Deformation of olivine at mantle pressure using D-DIA*, Eur. J. Mineral. 18 (2006), pp. 7–19.

[30] P. Raterron, J. Girard, and J. Chen, *Activities of olivine slip systems in the upper mantle*, Phys. Earth Planet. Int. 200–201 (2012), pp. 105–112.

[31] P.B. Hirsch, *The interpretation of the slip pattern in terms of dislocation movements*, J. Inst. Metals. 86 (1957), pp. 1957–1958.

[32] J. Durinck, B. Devincre, L. Kubin, and P. Cordier, *Modeling the plastic deformation of olivine by dislocation dynamics simulations*, Am. Mineral. 92 (2007), pp. 1346–1357.

[33] J.P. Morniroli, D. Vankieken, and L. Winter, *Electron Diffraction. Dedicated Software to Kinematicaly Simulate CBED Patterns*, USTL, Lille, 1994.

[34] J.P. Poirier, *Creep of Crystals. High-Temperature Deformation Processes in Metals, Ceramics and Minerals*, Cambridge University Press, Cambridge, 1985.

[35] F. Boioli, A. Tommasi, P. Cordier, S. Demouchy, and A. Mussi, *Low steady-state stresses in the cold lithospheric mantle inferred from dislocation dynamics models of dislocation creep in olivine*, Earth Planet. Sci. Lett. 432 (2015), pp. 232–242.

[36] B. Bakó, E. Clouet, L. Dupuy, and M. Blétry, *Dislocation dynamics simulations with climb: Kinetics of dislocation loop coarsening controlled by bulk diffusion*, Philos. Mag. 91 (2011), pp. 3173–3191.

[37] K.P.D. Lagerlöf, T.E. Mitchell, and A.H. Heuer, *Energetics of the break-up of dislocation dipoles into prismatic loops*, Acta Metall. Mater. 37 (1989), pp. 3315–3325.

[38] R. Madec, B. Devincre, L. Kubin, T. Hoc, and D. Rodney, *The role of collinear interaction in dislocation-induced hardening*, Science 301 (2003), pp. 1879–1882.